LUND UNIVERSITY

Nuclear-modification factor for open-heavy-flavor production at forward rapidity in Cu plus Cu collisions at root s(NN)=200 GeV

Adare, A.; Afanasiev, S.; Aidala, C.; Ajitanand, N. N.; Akiba, Y.; Al-Bataineh, H.; Alexander, J.; Aoki, K.; Aphecetche, L.; Armendariz, R.; Aronson, S. H.; Asai, J.; Atomssa, E. T.; Averbeck, R.; Awes, T. C.; Azmoun, B.; Babintsev, V.; Baksay, G.; Baksay, L.; Baldisseri, A.; Barish, K. N.; Barnes, P. D.; Bassalleck, B.; Bathe, S.; Batsouli, S.; Baublis, V.; Bazilevsky, A.; Belikov, S.; Bennett, R.; Berdnikov, Y.; Bickley, A. A.; Boissevain, J. G.; Borel, H.; Boyle, K.; Brooks, M. L.; Buesching, H.; Bumazhnov, V.; Bunce, G.; Butsyk, S.; Campbell, S.; Chang, B. S.; Charvet, J. -L.; Chernichenko, S.; Chi, C. Y.; Chiba, J.; Chiu, M.; Choi, I. J.; Chujo, T.; Chung, P.; Churyn, A.

Published in:
Physical Review C (Nuclear Physics)

DOI:
10.1103/PhysRevC.86.024909

2012

Link to publication

Citation for published version (APA):
Adare, A., Afanasiev, S., Aidala, C., Ajitanand, N. N., Akiba, Y., Al-Bataineh, H., Alexander, J., Aoki, K., Aphecetche, L., Armendariz, R., Aronson, S. H., Asai, J., Atomssa, E. T., Averbeck, R., Awes, T. C., Azmoun, B., Babintsev, V., Baksay, G., Baksay, L., ... Zolin, L. (2012). Nuclear-modification factor for open-heavy-flavor production at forward rapidity in Cu plus Cu collisions at root s(NN)=200 GeV. *Physical Review C (Nuclear Physics)*, *86*(2). https://doi.org/10.1103/PhysRevC.86.024909

Total number of authors:
377

General rights
Unless other specific re-use rights are stated the following general rights apply:
Copyright and moral rights for the publications made accessible in the public portal are retained by the authors and/or other copyright owners and it is a condition of accessing publications that users recognise and abide by the legal requirements associated with these rights.
• Users may download and print one copy of any publication from the public portal for the purpose of private study or research.
• You may not further distribute the material or use it for any profit-making activity or commercial gain
• You may freely distribute the URL identifying the publication in the public portal

Read more about Creative commons licenses: https://creativecommons.org/licenses/

Take down policy
If you believe that this document breaches copyright please contact us providing details, and we will remove access to the work immediately and investigate your claim.

Download date: 04. Jul. 2025

LUND UNIVERSITY

PO Box 117
221 00 Lund
+46 46-222 00 00

Nuclear-modification factor for open-heavy-flavor production at forward rapidity in Cu + Cu collisions at $\sqrt{s_{NN}} = 200$ GeV

A. Adare,[9] S. Afanasiev,[24] C. Aidala,[10] N. N. Ajitanand,[49] Y. Akiba,[43,44] H. Al-Bataineh,[38] J. Alexander,[49] K. Aoki,[28,43] L. Aphecetche,[51] R. Armendariz,[38] S. H. Aronson,[4] J. Asai,[44] E. T. Atomssa,[29] R. Averbeck,[50] T. C. Awes,[39] B. Azmoun,[4] V. Babintsev,[19] G. Baksay,[15] L. Baksay,[15] A. Baldisseri,[12] K. N. Barish,[5] P. D. Barnes,[31,*] B. Bassalleck,[37] S. Bathe,[5] S. Batsouli,[39] V. Baublis,[42] A. Bazilevsky,[4] S. Belikov,[4,*] R. Bennett,[50] Y. Berdnikov,[46] A. A. Bickley,[9] J. G. Boissevain,[31] H. Borel,[12] K. Boyle,[50] M. L. Brooks,[31] H. Buesching,[4] V. Bumazhnov,[19] G. Bunce,[4,44] S. Butsyk,[31,50] S. Campbell,[50] B. S. Chang,[59] J.-L. Charvet,[12] S. Chernichenko,[19] C. Y. Chi,[10] J. Chiba,[25] M. Chiu,[20] I. J. Choi,[59] T. Chujo,[55] P. Chung,[49] A. Churyn,[19] V. Cianciolo,[39] C. R. Cleven,[17] B. A. Cole,[10] M. P. Comets,[40] P. Constantin,[31] M. Csanád,[14] T. Csörgő,[58] T. Dahms,[50] K. Das,[16] G. David,[4] M. B. Deaton,[1] K. Dehmelt,[15] H. Delagrange,[51] A. Denisov,[19] D. d'Enterria,[10] A. Deshpande,[44,50] E. J. Desmond,[4] O. Dietzsch,[47] A. Dion,[50] M. Donadelli,[47] O. Drapier,[29] A. Drees,[50] A. K. Dubey,[57] A. Durum,[19] V. Dzhordzhadze,[5] Y. V. Efremenko,[39] J. Egdemir,[50] F. Ellinghaus,[9] W. S. Emam,[5] A. Enokizono,[30] H. En'yo,[43,44] S. Esumi,[54] K. O. Eyser,[5] D. E. Fields,[37,44] M. Finger,[6,24] M. Finger Jr.,[6,24] F. Fleuret,[29] S. L. Fokin,[27] Z. Fraenkel,[57,*] J. E. Frantz,[50] A. Franz,[4] A. D. Frawley,[16] K. Fujiwara,[43] Y. Fukao,[28,43] T. Fusayasu,[36] S. Gadrat,[32] A. Garishvili,[52] I. Garishvili,[30,52] A. Glenn,[9] H. Gong,[50] M. Gonin,[29] J. Gosset,[12] Y. Goto,[43,44] R. Granier de Cassagnac,[29] N. Grau,[23] S. V. Greene,[55] M. Grosse Perdekamp,[20,44] T. Gunji,[8] H.-Å. Gustafsson,[33,*] T. Hachiya,[18] A. Hadj Henni,[51] C. Haegemann,[37] J. S. Haggerty,[4] H. Hamagaki,[8] R. Han,[41] H. Harada,[18] E. P. Hartouni,[30] K. Haruna,[18] E. Haslum,[33] R. Hayano,[8] X. He,[17] M. Heffner,[30] T. K. Hemmick,[50] T. Hester,[5] H. Hiejima,[20] J. C. Hill,[23] R. Hobbs,[37] M. Hohlmann,[15] W. Holzmann,[49] K. Homma,[18] B. Hong,[26] T. Horaguchi,[43,53] D. Hornback,[52] T. Ichihara,[43,44] H. Iinuma,[28,43] K. Imai,[28,43] M. Inaba,[54] Y. Inoue,[43,45] D. Isenhower,[1] L. Isenhower,[1] M. Ishihara,[43] T. Isobe,[8] M. Issah,[49] A. Isupov,[24] B. V. Jacak,[50,†] J. Jia,[10] J. Jin,[10] O. Jinnouchi,[44] B. M. Johnson,[4] K. S. Joo,[35] D. Jouan,[40] F. Kajihara,[8] S. Kametani,[8,56] N. Kamihara,[43] J. Kamin,[50] M. Kaneta,[44] J. H. Kang,[59] H. Kanou,[43,53] D. Kawall,[44] A. V. Kazantsev,[27] A. Khanzadeev,[42] J. Kikuchi,[56] D. H. Kim,[35] D. J. Kim,[59] E. Kim,[48] E. Kinney,[9] Á. Kiss,[14] E. Kistenev,[4] A. Kiyomichi,[43] J. Klay,[30] C. Klein-Boesing,[34] L. Kochenda,[42] V. Kochetkov,[19] B. Komkov,[42] M. Konno,[54] D. Kotchetkov,[5] A. Kozlov,[57] A. Král,[11] A. Kravitz,[10] J. Kubart,[6,22] G. J. Kunde,[31] N. Kurihara,[8] K. Kurita,[43,45] M. J. Kweon,[26] Y. Kwon,[59,52] G. S. Kyle,[38] R. Lacey,[49] Y. S. Lai,[10] J. G. Lajoie,[23] A. Lebedev,[23] D. M. Lee,[31] M. K. Lee,[59] T. Lee,[48] M. J. Leitch,[31] M. A. L. Leite,[47] B. Lenzi,[47] X. Li,[7] T. Liška,[11] A. Litvinenko,[24] M. X. Liu,[31] B. Love,[55] D. Lynch,[4] C. F. Maguire,[55] Y. I. Makdisi,[3] A. Malakhov,[24] M. D. Malik,[37] V. I. Manko,[27] Y. Mao,[41,43] L. Mašek,[6,22] H. Masui,[54] F. Matathias,[10] M. McCumber,[50] P. L. McGaughey,[31] Y. Miake,[54] P. Mikeš,[6,22] K. Miki,[54] T. E. Miller,[55] A. Milov,[50] S. Mioduszewski,[4] M. Mishra,[2] J. T. Mitchell,[4] M. Mitrovski,[49] A. Morreale,[5] D. P. Morrison,[4] T. V. Moukhanova,[27] D. Mukhopadhyay,[55] J. Murata,[43,45] S. Nagamiya,[25] Y. Nagata,[54] J. L. Nagle,[9] M. Naglis,[57] I. Nakagawa,[43,44] Y. Nakamiya,[18] T. Nakamura,[18] K. Nakano,[43,53] J. Newby,[30] M. Nguyen,[50] B. E. Norman,[31] R. Nouicer,[4] A. S. Nyanin,[27] E. O'Brien,[4] S. X. Oda,[8] C. A. Ogilvie,[23] H. Ohnishi,[43] M. Oka,[54] K. Okada,[44] O. O. Omiwade,[1] A. Oskarsson,[33] M. Ouchida,[18] K. Ozawa,[8] R. Pak,[4] D. Pal,[55] A. P. T. Palounek,[31] V. Pantuev,[21,50] V. Papavassiliou,[38] J. Park,[48] W. J. Park,[26] S. F. Pate,[38] H. Pei,[23] J.-C. Peng,[20] H. Pereira,[12] V. Peresedov,[24] D. Yu. Peressounko,[27] C. Pinkenburg,[4] M. L. Purschke,[4] A. K. Purwar,[31] H. Qu,[17] J. Rak,[37] A. Rakotozafindrabe,[29] I. Ravinovich,[57] K. F. Read,[39,52] S. Rembeczki,[15] M. Reuter,[50] K. Reygers,[34] V. Riabov,[42] Y. Riabov,[42] G. Roche,[32] A. Romana,[29,*] M. Rosati,[23] S. S. E. Rosendahl,[33] P. Rosnet,[32] P. Rukoyatkin,[24] V. L. Rykov,[43] B. Sahlmueller,[34] N. Saito,[28,43,44] T. Sakaguchi,[4] S. Sakai,[54] H. Sakata,[18] V. Samsonov,[42] S. Sato,[25] S. Sawada,[25] J. Seele,[9] R. Seidl,[20] V. Semenov,[19] R. Seto,[5] D. Sharma,[57] I. Shein,[19] A. Shevel,[42,49] T.-A. Shibata,[43,53] K. Shigaki,[18] M. Shimomura,[54] K. Shoji,[28,43] A. Sickles,[50] C. L. Silva,[47] D. Silvermyr,[39] C. Silvestre,[12] K. S. Sim,[26] C. P. Singh,[2] V. Singh,[2] S. Skutnik,[23] M. Slunečka,[6,24] A. Soldatov,[19] R. A. Soltz,[30] W. E. Sondheim,[31] S. P. Sorensen,[52] I. V. Sourikova,[4] F. Staley,[12] P. W. Stankus,[39] E. Stenlund,[33] M. Stepanov,[38] A. Ster,[58] S. P. Stoll,[4] T. Sugitate,[18] C. Suire,[40] J. Sziklai,[58] T. Tabaru,[44] S. Takagi,[54] E. M. Takagui,[47] A. Taketani,[43,44] Y. Tanaka,[36] K. Tanida,[43,44,48] M. J. Tannenbaum,[4] A. Taranenko,[49] P. Tarján,[13] T. L. Thomas,[37] M. Togawa,[28,43] A. Toia,[50] J. Tojo,[43] L. Tomášek,[22] H. Torii,[43] R. S. Towell,[1] V-N. Tram,[29] I. Tserruya,[57] Y. Tsuchimoto,[18] C. Vale,[23] H. Valle,[55] H. W. van Hecke,[31] J. Velkovska,[55] R. Vértesi,[13] A. A. Vinogradov,[27] M. Virius,[11] V. Vrba,[22] E. Vznuzdaev,[42] M. Wagner,[28,43] D. Walker,[50] X. R. Wang,[38] Y. Watanabe,[43,44] J. Wessels,[34] S. N. White,[4] D. Winter,[10] C. L. Woody,[4] M. Wysocki,[9] W. Xie,[44] Y. L. Yamaguchi,[56] A. Yanovich,[19] Z. Yasin,[5] J. Ying,[17] S. Yokkaichi,[43,44] G. R. Young,[39] I. Younus,[37] I. E. Yushmanov,[27] W. A. Zajc,[10] O. Zaudtke,[34] C. Zhang,[39] S. Zhou,[7] J. Zimányi,[58,*] and L. Zolin[24]

(PHENIX Collaboration)

[1]*Abilene Christian University, Abilene, Texas 79699, USA*

[2]*Department of Physics, Banaras Hindu University, Varanasi 221005, India*

[3]*Collider-Accelerator Department, Brookhaven National Laboratory, Upton, New York 11973-5000, USA*

[4]*Brookhaven National Laboratory, Upton, New York 11973-5000, USA*

[5]*University of California—Riverside, Riverside, California 92521, USA*

[6]*Charles University, Ovocný trh 5, Praha 1, 116 36 Prague, Czech Republic*

[7]*Science and Technology on Nuclear Data Laboratory, China Institute of Atomic Energy, Beijing 102413, P. R. China*

[8]*Center for Nuclear Study, Graduate School of Science, University of Tokyo, 7-3-1 Hongo, Bunkyo, Tokyo 113-0033, Japan*

 ©2012 American Physical Society

[9]*University of Colorado, Boulder, Colorado 80309, USA*
[10]*Columbia University, New York, New York 10027 and Nevis Laboratories, Irvington, New York 10533, USA*
[11]*Czech Technical University, Zikova 4, 166 36 Prague 6, Czech Republic*
[12]*Dapnia, CEA Saclay, F-91191 Gif-sur-Yvette, France*
[13]*Debrecen University, H-4010 Debrecen, Egyetem tér 1, Hungary*
[14]*ELTE, Eötvös Loránd University, H-1117 Budapest, Pázmány P. s. 1/A, Hungary*
[15]*Florida Institute of Technology, Melbourne, Florida 32901, USA*
[16]*Florida State University, Tallahassee, Florida 32306, USA*
[17]*Georgia State University, Atlanta, Georgia 30303, USA*
[18]*Hiroshima University, Kagamiyama, Higashi-Hiroshima 739-8526, Japan*
[19]*IHEP Protvino, State Research Center of Russian Federation, Institute for High Energy Physics, Protvino 142281, Russia*
[20]*University of Illinois at Urbana-Champaign, Urbana, Illinois 61801, USA*
[21]*Institute for Nuclear Research of the Russian Academy of Sciences, prospekt 60-letiya Oktyabrya 7a, Moscow 117312, Russia*
[22]*Institute of Physics, Academy of Sciences of the Czech Republic, Na Slovance 2, 182 21 Prague 8, Czech Republic*
[23]*Iowa State University, Ames, Iowa 50011, USA*
[24]*Joint Institute for Nuclear Research, 141980 Dubna, Moscow Region, Russia*
[25]*KEK, High Energy Accelerator Research Organization, Tsukuba, Ibaraki 305-0801, Japan*
[26]*Korea University, Seoul 136-701, Korea*
[27]*Russian Research Center "Kurchatov Institute," Moscow 123098, Russia*
[28]*Kyoto University, Kyoto 606-8502, Japan*
[29]*Laboratoire Leprince-Ringuet, Ecole Polytechnique, CNRS-IN2P3, Route de Saclay, F-91128 Palaiseau, France*
[30]*Lawrence Livermore National Laboratory, Livermore, California 94550, USA*
[31]*Los Alamos National Laboratory, Los Alamos, New Mexico 87545, USA*
[32]*LPC, Université Blaise Pascal, CNRS-IN2P3, Clermont-Fd, 63177 Aubiere Cedex, France*
[33]*Department of Physics, Lund University, Box 118, SE-221 00 Lund, Sweden*
[34]*Institut für Kernphysik, University of Muenster, D-48149 Muenster, Germany*
[35]*Myongji University, Yongin, Kyonggido 449-728, Korea*
[36]*Nagasaki Institute of Applied Science, Nagasaki-shi, Nagasaki 851-0193, Japan*
[37]*University of New Mexico, Albuquerque, New Mexico 87131, USA*
[38]*New Mexico State University, Las Cruces, New Mexico 88003, USA*
[39]*Oak Ridge National Laboratory, Oak Ridge, Tennessee 37831, USA*
[40]*IPN-Orsay, Universite Paris Sud, CNRS-IN2P3, BP1, F-91406 Orsay, France*
[41]*Peking University, Beijing 100871, P. R. China*
[42]*PNPI, Petersburg Nuclear Physics Institute, Gatchina, Leningrad region 188300, Russia*
[43]*RIKEN Nishina Center for Accelerator-Based Science, Wako, Saitama 351-0198, Japan*
[44]*RIKEN BNL Research Center, Brookhaven National Laboratory, Upton, New York 11973-5000, USA*
[45]*Physics Department, Rikkyo University, 3-34-1 Nishi-Ikebukuro, Toshima, Tokyo 171-8501, Japan*
[46]*Saint Petersburg State Polytechnic University, St. Petersburg 195251, Russia*
[47]*Universidade de São Paulo, Instituto de Física, Caixa Postal 66318, São Paulo CEP 05315-970, Brazil*
[48]*Seoul National University, Seoul, Korea*
[49]*Chemistry Department, Stony Brook University, SUNY, Stony Brook, New York 11794-3400, USA*
[50]*Department of Physics and Astronomy, Stony Brook University, SUNY, Stony Brook, New York 11794-3400, USA*
[51]*SUBATECH (Ecole des Mines de Nantes, CNRS-IN2P3, Université de Nantes) BP 20722-44307, Nantes, France*
[52]*University of Tennessee, Knoxville, Tennessee 37996, USA*
[53]*Department of Physics, Tokyo Institute of Technology, Oh-okayama, Meguro, Tokyo 152-8551, Japan*
[54]*Institute of Physics, University of Tsukuba, Tsukuba, Ibaraki 305, Japan*
[55]*Vanderbilt University, Nashville, Tennessee 37235, USA*
[56]*Waseda University, Advanced Research Institute for Science and Engineering, 17 Kikui-cho, Shinjuku-ku, Tokyo 162-0044, Japan*
[57]*Weizmann Institute, Rehovot 76100, Israel*
[58]*Institute for Particle and Nuclear Physics, Wigner Research Centre for Physics, Hungarian Academy of Sciences (Wigner RCP, RMKI) H-1525 Budapest 114, P.O. Box 49, Budapest, Hungary*
[59]*Yonsei University, IPAP, Seoul 120-749, Korea*

(Received 3 April 2012; published 20 August 2012)

Background: Heavy-flavor production in $p + p$ collisions is a good test of perturbative-quantum-chromodynamics (pQCD) calculations. Modification of heavy-flavor production in heavy-ion collisions relative to binary-collision scaling from $p + p$ results, quantified with the nuclear-modification factor (R_{AA}), provides information on both cold- and hot-nuclear-matter effects. Midrapidity heavy-flavor R_{AA} measurements at the

Relativistic Heavy Ion Collider have challenged parton-energy-loss models and resulted in upper limits on the viscosity-entropy ratio that are near the quantum lower bound. Such measurements have not been made in the forward-rapidity region.

Purpose: Determine transverse-momentum (p_T) spectra and the corresponding R_{AA} for muons from heavy-flavor meson decay in $p + p$ and Cu + Cu collisions at $\sqrt{s_{NN}} = 200$ GeV and $y = 1.65$.

Method: Results are obtained using the semileptonic decay of heavy-flavor mesons into negative muons. The PHENIX muon-arm spectrometers measure the p_T spectra of inclusive muon candidates. Backgrounds, primarily due to light hadrons, are determined with a Monte Carlo calculation using a set of input hadron distributions tuned to match measured-hadron distributions in the same detector and statistically subtracted.

Results: The charm-production cross section in $p + p$ collisions at $\sqrt{s} = 200$ GeV, integrated over p_T and in the rapidity range $1.4 < y < 1.9$, is found to be $d\sigma_{c\bar{c}}/dy = 0.139 \pm 0.029$ (stat) $^{+0.051}_{-0.058}$ (syst) mb. This result is consistent with a perturbative fixed-order-plus-next-to-leading-log calculation within scale uncertainties and is also consistent with expectations based on the corresponding midrapidity charm-production cross section measured by PHENIX. The R_{AA} for heavy-flavor muons in Cu + Cu collisions is measured in three centrality bins for $1 < p_T < 4$ GeV/c. Suppression relative to binary-collision scaling ($R_{AA} < 1$) increases with centrality.

Conclusions: Within experimental and theoretical uncertainties, the measured charm yield in $p + p$ collisions is consistent with state-of-the-art pQCD calculations. Suppression in central Cu + Cu collisions suggests the presence of significant cold-nuclear-matter effects and final-state energy loss.

DOI: 10.1103/PhysRevC.86.024909 PACS number(s): 25.75.Dw

I. INTRODUCTION

Understanding the energy loss mechanism for partons moving through the hot dense partonic matter produced in heavy-ion collisions at the Relativistic Heavy Ion Collider (RHIC) and the Large Hadron Collider (LHC) is a key priority in the field of heavy-ion collision physics [1,2]. Production of heavy quarks in heavy-ion collisions can serve as an important tool for better understanding properties of the dense matter created in such collisions. In particular, because of their large mass, heavy quarks are almost exclusively produced in the early stages of heavy-ion collisions and, therefore, can serve as a probe of the subsequently created medium. The large mass scale associated with the production of heavy quarks also allows one to test perturbative quantum chromodynamics-(pQCD) based theoretical models describing high-energy collisions.

Recent measurements of heavy-quark production in heavy-ion collisions [3–5] exhibit a suppression, which is larger than expected and not easily reconciled with early theoretical predictions [6,7]. In these calculations the dominant energy loss mechanism for fast partons is gluon bremsstrahlung [8,9]. In this context, it was predicted that heavy quarks would lose less energy than light quarks due to the so-called *dead-cone effect* [10]. The disagreement between this prediction and experimental results led to a consideration of alternative in-medium parton energy loss mechanisms, assumed earlier to have a small effect on heavy quarks compared to radiative energy loss. In particular, it was suggested that heavy quarks can lose a significant amount of their energy through elastic collisions with in-medium partons (collisional energy loss mechanism) [11–13], especially in the intermediate transverse-momentum range ($p_T \approx 3$–8 GeV/c) in which most of the RHIC heavy-flavor measurements are performed. Additional mechanisms for in-medium energy loss for heavy quarks have also been suggested [14,15]. Despite recent progress, a universal theoretical framework precisely describing the production of heavy quarks and their subsequent interactions with the partonic medium created in heavy-ion collisions is still needed, along with accurate measurements of heavy-quark production in heavy-ion collisions, which are critical to test and constrain the theoretical predictions.

Hidden heavy-flavor (J/ψ) production has also been extensively measured in heavy-ion collisions [16,17]. The production of J/ψ mesons is expected to be affected by the formation of a quark-gluon plasma due to the interplay of several competing mechanisms, including suppression due to a color screening mechanism similar to the Debye screening in QED [18] and enhancement due to the coalescence of uncorrelated $c\bar{c}$ pairs from the hot medium [19–21]. The magnitude of such an enhancement depends strongly on the production cross section of heavy flavor in heavy-ion collisions, measurements of which are, therefore, essential to the interpretation of heavy quarkonia results.

A well-established observable for quantifying medium effects in heavy-ion collisions is the nuclear-modification factor, R_{AA},

$$R_{AA} = \frac{1}{N_{\rm coll}} \frac{\sigma_{AA}}{\sigma_{pp}}, \tag{1}$$

where σ_{AA} and σ_{pp} are the invariant cross sections for a given process in $A + A$ collisions and $p + p$ collisions, respectively, and $N_{\rm coll}$ is the average number of nucleon-nucleon collisions in the $A + A$ collision, evaluated using a simple geometrical description of the A nucleus [22].

For processes that are sufficiently hard (characterized by large energy transfer), R_{AA} is expected to be equal to unity in the absence of nuclear effects. A value smaller (larger) than unity indicates suppression (enhancement) of the observed yield in $A + A$ collisions relative to expectations based on $p + p$ collision results and binary-collision scaling.

Open heavy-flavor production has been measured by the PHENIX experiment at midrapidity ($|\eta| < 0.35$) [3]. This

*Deceased.
†PHENIX spokesperson: jacak@skipper.physics.sunysb.edu

paper presents the measurement of heavy-flavor production at forward rapidity ($1.4 < |\eta| < 1.9$) in Cu + Cu and $p + p$ collisions, and the resulting R_{AA}, using negatively charged muons from the semileptonic decay of heavy-flavor mesons. Due to the limited transverse-momentum range of the measurement ($1 < p_T < 7$ GeV/c), the contribution from beauty to the heavy-flavor yields is expected to be negligible and only charm quarks are measured effectively.

The paper is organized as follows: Section II presents a short overview of the PHENIX detector subsystems relevant to these measurements followed by a description of the data sets and track selection criteria. Section III presents a detailed description of the methodology for measuring the invariant cross section in $p + p$ collisions and R_{AA} in Cu + Cu collisions for muons from heavy-flavor meson decays. Results are presented in Sec. IV and compared to existing measurements as well as theoretical predictions in Sec. V.

II. EXPERIMENTAL SETUP AND DATA SETS

A. The PHENIX experiment

The PHENIX experiment is equipped with two muon spectrometers [23], shown in Fig. 1, that provide pion rejection at the level of 2.5×10^{-4} in the pseudorapidity range $-1.2 < \eta < -2.2$ (south muon arm) and $1.2 < \eta < 2.4$ (north muon arm) over the full azimuth. Each muon arm is located behind a thick copper and iron absorber and composes three stations of cathode strip chambers (the Muon Tracker, or MuTr), surrounded by a radial magnetic field, and five "gaps" (numbered 0 to 4) consisting of a plane of steel absorber and a plane of Iarrocci tubes (the Muon Identifier, or MuID). The MuTr measures the momentum of charged particles by tracking their motion in the surrounding magnetic field. Matching the momentum of the particles reconstructed in the MuTr to the penetration depth of the particle in the MuID (that is, the last MuID gap a given particle reaches) is the primary tool used to identify muons with respect to the residual hadronic background. Measured muons must penetrate 8 to 11 interaction lengths in total to reach the last gap of the MuID. This corresponds to a reduction of the muon longitudinal momentum (along the beam axis) of $\delta p_z = 2.3(2.45)$ GeV/c in the south (north) muon arm. The MuID is also used in the online data acquisition to trigger on collisions that contain one or more muon candidates.

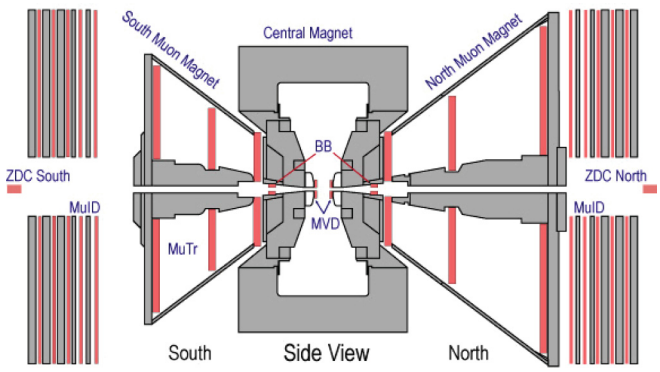

FIG. 1. (Color online) Side view of the PHENIX muon detectors (2005).

Also used in this analysis are the Beam-Beam Counters (BBC) [24], which comprise two arrays of 64 quartz Čerenkov detectors that surround the beam, one on each side of the interaction point. The BBCs measure charged particles produced during the collision in the pseudorapidity range $3 < |\eta| < 3.9$ and determine the collision's start time, vertex longitudinal position, and centrality (in Cu + Cu collisions). The BBCs also provide the minimum bias trigger.

B. Data sets

Two data sets, recorded in 2005, are used in this analysis: $p + p$ collisions and Cu + Cu collisions at a center-of-mass energy per nucleon-nucleon collision of $\sqrt{s_{NN}} = 200$ GeV.

The $p + p$ data used for this analysis have been recorded using two *muon enriched* triggers, in coincidence with the Minimum Bias (MB) trigger, which requires at least one hit in each of the BBCs and covers approximately 55% of the total $p + p$ inelastic cross section. These two muon triggers rely on the information recorded in the MuID. The first (*Deep*) trigger requires one or more muon candidates to reach the last plane of the MuID (Gap4), whereas the second, less strict, (*Shallow*) trigger requires one or more muon candidates to reach at least the third MuID gap (Gap2). The integrated luminosity sampled with these triggers and used for this analysis is 44.3 nb^{-1} (48.7 nb^{-1}) for the south (north) muon arm.

All Cu + Cu data used for this analysis have been recorded using the Minimum Bias trigger described above. For Cu + Cu collisions, this trigger covers approximately 94% of the total inelastic cross section. The integrated luminosity sampled with this trigger and used for this analysis is 0.11 nb^{-1}, using a total Cu + Cu inelastic cross section seen by the minimum bias trigger $\sigma^{\text{inel}}_{\text{Cu+Cu}} = 3.3$ b.

C. Centrality determination

The centrality of each Cu + Cu collision is determined by the total charge deposited in the BBCs. Three centrality bins are used for this analysis: 0–20%, 20–40% and 40–94%, where 0–20% represents the most central 20% of the collisions. For a given centrality bin, the average number of nucleon-nucleon collisions (N_{coll}) and the average number of participating nucleons (N_{part}) are estimated using a Glauber calculation [22] coupled to a model of the BBC response. Values of N_{coll} and N_{part} for the three centrality bins defined above are listed in Table I.

To ensure that the centrality bins are well defined, collisions are required to be within ±30 cm of the center of the PHENIX detector along the beam axis.

TABLE I. Centrality characterization variables for Cu + Cu collisions.

Centrality	0–20%	20–40%	40–94%
N_{coll}	151.8 ± 17.1	61.6 ± 6.6	11.23 ± 1.3
N_{part}	85.9 ± 2.3	45.2 ± 1.7	11.7 ± 0.6

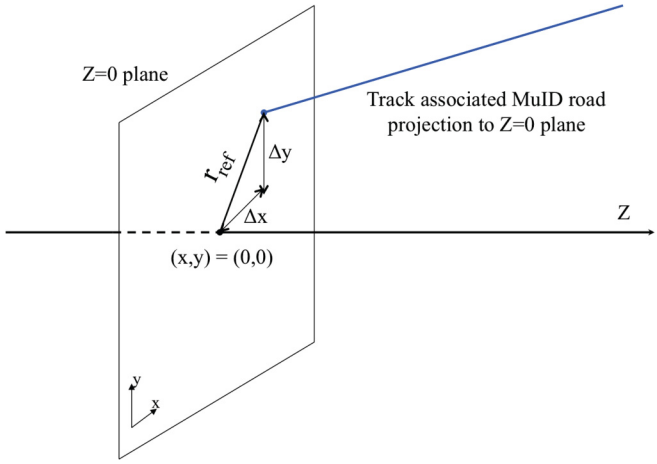

FIG. 2. (Color online) Schematic representation of $r_{\rm ref}$ variable.

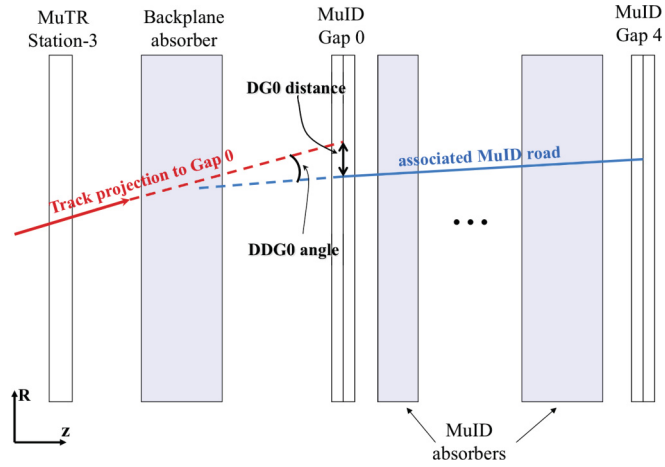

FIG. 3. (Color online) Schematic representation of track selection variables DG0 and DDG0.

D. Track selection

This section outlines the track-based selection variables.

$z_{\rm BBC}$ The event vertex longitudinal position is measured by the BBC detector. For low-momentum tracks ($p_T < 2$ GeV/c) reconstructed in the north (south) muon arm we demand $z_{\rm BBC} > 0$ ($z_{\rm BBC} < 0$). This arm-dependent cut improves the signal-to-background ratio because light hadrons produced during the collision have a probability to decay into a muon that increases with their distance from the front muon arm absorber, whereas muons from short-lived heavy-flavor hadrons have a yield that is independent of $z_{\rm BBC}$ (see also Sec. III C3).

$z_{\rm fit}$ The vertex longitudinal position of a track evaluated using a fit of the track position and momentum measured in the MuTr and extrapolated backward through the front absorber toward the interaction point, together with the BBC vertex measurement.

$N_{\rm hits}^{\rm MuTr}$ The total number of track hits in the three MuTr stations. A given track can have up to 16 MuTr hits.

$N_{\rm hits}^{\rm MuID}$ The total number of track hits in the five MuID gaps. A given track can have up to two hits in each gap (10 in total).

$r_{\rm ref}$ The distance to the beam axis of the track, as reconstructed in the MuID only, when extrapolated (backward) to $z = 0$ (illustrated in Fig. 2).

Road Slope The slope of the track, as reconstructed in the MuID only, measured at MuID Gap0: $\sqrt{(dx/dz)^2 + (dy/dz)^2}$. A cut applied to this variable eliminates combinatorial background generated in the high hit-density region closest to the beam pipe.

DG0 The distance between the track positions calculated in the MuTr and in the MuID, evaluated at the MuID Gap0 z position (see Fig. 3).

DDG0 The difference between the track angles calculated in the MuTr and in the MuID, evaluated at the MuID Gap0 z position (see Fig. 3).

δz The difference between the event vertex longitudinal position reconstructed by the BBC ($z_{\rm BBC}$) and the track longitudinal position provided by the track reconstruction algorithm: $\delta z = |z_{\rm BBC} - z_{\rm fit}|$.

p$\delta\theta$ The *effective* scattering angle of the track in the front absorber, $\delta\theta$, scaled by the average of the momentum measured at the vertex and at MuTr Station 1: $p = (p_{\rm vtx} + p_{\rm st1})/2$. The angle $\delta\theta$ is given by

$$\delta\theta = \cos^{-1}\left(\frac{\vec{p}_{\rm vtx}\cdot\vec{p}_{\rm st1}}{p_{\rm vtx}\cdot p_{\rm st1}}\right), \qquad (2)$$

where $\vec{p}_{\rm st1}$ is the momentum vector measured at Station 1 and $\vec{p}_{\rm vtx}$ is the momentum vector at the vertex. For a given track, $\delta\theta$ essentially measures the track deflection in the front absorber due mostly to multiple scattering and radiative energy loss, but also to the magnetic field upstream of Station 1. This deflection is expected to be inversely proportional to the track total momentum. Scaling the scattering angle $\delta\theta$ by the track momentum therefore ensures that the $p\delta\theta$ distribution is approximately Gaussian with a constant width for all p_T bins.

Cut values applied to these variables are, in some cases, p_T, species, and/or centrality dependent. Within a given p_T, species, and centrality bin, the same cut values are applied to both Monte Carlo simulations and real data.

Even after all cuts are applied to select *good quality* muon candidates, there remains a small contamination of misreconstructed tracks caused by (i) accidental combinations of hits in the muon tracker that do not correspond to a real particle and (ii) tracks arising from interactions between the beam and residual gas in the beam pipe or between the beam and beamline components.

These misreconstructed tracks, later denoted N_F, are not completely reproduced by experimental simulations and must be estimated and properly subtracted from the inclusive muon sample to evaluate the amount of muons from heavy-flavor decay. The method by which N_F is estimated is based on the distributions of the $p\delta\theta$ and δz variables and is described in more detail in Sec. III B.

Note: Positive muons are not used in this analysis due to a poorer signal-background ratio resulting from the fact that both antiprotons and negative kaons are more strongly suppressed by the MuTr front absorbers than their positive counterparts. The rapidity interval used for this measurement is smaller than the rapidity coverage of the PHENIX muon spectrometers ($1.2 < |\eta| < 2.2$) to reduce uncertainties in the acceptance calculation.

III. METHOD FOR THE MEASUREMENT OF HEAVY-FLAVOR MUONS

A. Overview

The methodology used to measure heavy-flavor muon (i.e., muons from heavy-flavor meson decay) production in $p+p$ and Cu + Cu collisions is described in this section. This analysis is a refinement of techniques originally developed in Refs. [25–27].

For both $p+p$ and Cu + Cu collisions the double differential heavy flavor muon invariant yield is defined by

$$\frac{d^2N^{\mu}}{2\pi\, p_T dp_T d\eta} = \frac{1}{2\pi\, p_T \Delta p_T \Delta\eta} \frac{N_I - N_C - N_F}{N_{\rm evt}\epsilon_{\rm BBC}^{c\bar{c}\to\mu} A\epsilon}, \quad (3)$$

where N_I is the total number of muon candidates in the bin, consisting of the tracks that reach the last gap of the MuID (Gap4) and pass all track selection criteria; N_C is the number of tracks corresponding to the irreducible hadronic background, as determined using a hadron cocktail approach (Sec. III C); N_F is the estimated number of misreconstructed tracks that pass the track selection cuts accidentally (Sec. III B); $N_{\rm evt}$ is the number of events; $A\epsilon$ is the detector acceptance and efficiency correction (Sec. III E); and $\epsilon_{\rm BBC}^{c\bar{c}\to\mu}$ is the BBC trigger efficiency for events in which a heavy-flavor muon at forward rapidity is present. This efficiency amounts to 79% (100%) in $p+p$ (Cu + Cu) collisions.

The $p+p$ and Cu + Cu invariant yields determined with Eq. (3) can be used directly to determine the heavy-flavor muon R_{AA} [Eq. (1)]. However, in order to minimize the systematic uncertainty associated with the estimate of the hadronic background by canceling the part of this uncertainty that is correlated between the $p+p$ and the Cu + Cu analyses, R_{AA} is calculated separately for a given $i^{\rm th}$ version of the Monte Carlo simulation of hadron cocktail used in the estimate of N_C,

$$R_{\rm AA}^i = \frac{1}{N_{\rm coll}} \left(\frac{d^2N_{\rm Cu+Cu}/dp_T d\eta}{d^2N_{pp}/dp_T d\eta} \right)^i. \quad (4)$$

The final value for R_{AA} is then determined by taking the mean of the values obtained for the different cocktails, each weighted by its ability to reproduce measured data, as discussed in Sec. III G.

B. Contamination from misreconstructed tracks

N_F, the number of misreconstructed tracks that accidentally pass all track quality cuts, is estimated using the $p\delta\theta$ distribution inside and outside of the δz cut defined in Sec. II D. These two distributions are shown in Fig. 4(a). The distribution

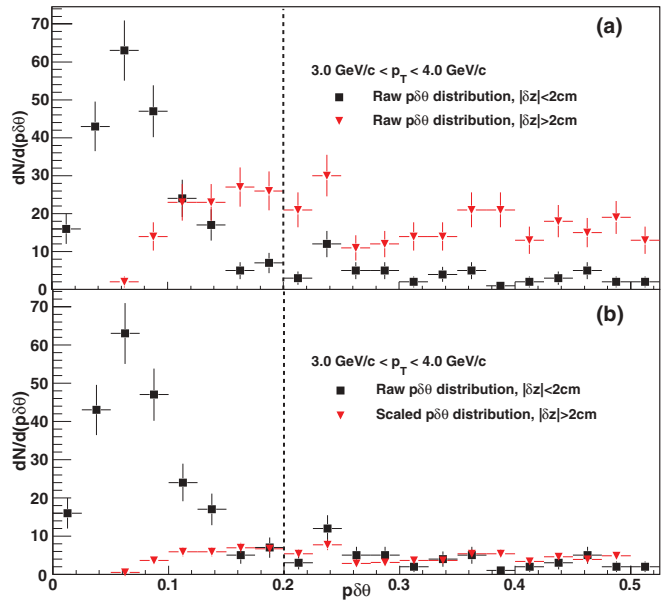

FIG. 4. (Color online) $p\delta\theta$ distributions for negatively charged inclusive muon candidates, $3 < p_T < 4$ GeV/c, measured in the north muon arm for the 20% most central Cu + Cu collisions. (a) Comparison of the distribution inside (black squares) and outside (red triangles) the δz cut. (b) Comparison of the same distributions, but the distribution outside the δz cut (red triangles) is normalized to the distribution inside the δz cut (black squares) in the region $p\delta\theta > p\delta\theta_{\rm max}$. In both panels, the vertical dashed line corresponds to $p\delta\theta_{\rm max}$.

inside the δz cut (black squares) shows two contributions: a peak at $p\delta\theta = 0.05$ rad GeV/c, corresponding to the expected multiple scattering of muons in the front absorber, and a tail out to large values of $p\delta\theta$. In the distribution outside the δz cut (red triangles), the signal peak has disappeared, and only the tail remains. Note that the tail extends below the $p\delta\theta$ cut; this is the N_F contribution. Using the fact that the shape of this tail appears to be the same on both sides of the δz cut, one can estimate N_F using

$$N_F = \alpha N_F', \quad (5)$$

where N_F' is the number of tracks with $p\delta\theta < p\delta\theta_{\rm max}$ but $\delta z > \delta z_{\rm max}$, and α normalizes the tails of the two distributions above the $p\delta\theta$ cut,

$$\alpha = \frac{N(p\delta\theta > p\delta\theta_{\rm max}, \delta z < \delta z_{\rm max})}{N(p\delta\theta > p\delta\theta_{\rm max}, \delta z > \delta z_{\rm max})}. \quad (6)$$

Figure 4(b) shows the $p\delta\theta$ distribution inside the δz cut [black squares, identical to the corresponding distribution in Fig. 4(a)] and the distribution outside the δz cut [red triangles from Fig. 4(a)] after scaling by α [Eq. (6)].

Using Eqs. (5) and (6), it is found that N_F amounts to less than 1% of the inclusive muon sample in the lowest-p_T bin ($1 < p_T < 1.5$ GeV/c) and increases with p_T up to about 5% (12%) for the highest-p_T bins in $p+p$ (central Cu + Cu) collisions. Uncertainties on these estimates are negligible in the final results.

C. Hadron cocktail

Charged pions and kaons are the largest source of particles in the PHENIX muon arms. Other species (p, $\bar{p}$, K_s^0, K_L^0) have small but nonzero contributions. Altogether, these light hadrons constitute the main background source for the measurement of muons from heavy-flavor meson decay.

One can define three contributions to this background, depending on how the particles enter the muon spectrometer:

Decay muons. Light hadrons that decay into muons before reaching the first absorber material. Since these particles enter the spectrometer as muons, a fraction of them also penetrate all the absorber layers of the MuID and enter the pool of inclusive muon candidates.

Punch-through hadrons. Hadrons produced at the collision vertex that do not decay but penetrate all MuID absorber layers, thus also being (incorrectly) identified as muons.

Decay-in-MuTr. Hadrons produced at the collision vertex that penetrate the muon arm front absorber and decay into a muon inside the MuTr tracking volume, with the decay muon then passing through the rest of the MuTr and the MuID. Most such particles are simply not reconstructed because of the decay angle between the primary hadron and the decay muon. However, some can be reconstructed, usually with an incorrect momentum assigned to the track. Due to the exponential p_T distribution, even a small number of such tracks can form a significant background at high p_T but for the p_T range in this analysis this contribution is small.

While decay muons cannot be distinguished from punch-through hadrons and heavy-flavor muons on an event-by-event basis, their production exhibits a strong vertex dependence, as illustrated in Fig. 5. This feature plays a key role in constraining heavy-flavor background (Sec. III C3).

A series of Monte Carlo simulations ("hadron cocktail packages") are used to estimate the overall background due to light hadron sources. The construction of a given hadronic cocktail package involves the following steps:

(i) Generate a primary hadron sample based on parameterized p_T and y distributions (Sec. III C1).
(ii) Propagate these hadrons through the muon spectrometer using the complete GEANT3 [28] PHENIX simulation. Each hadron cocktail package uses one of the two hadron shower codes provided by GEANT3: G-FLUKA or GHEISHA with a scaled value of the hadron-iron interaction cross section (Sec. III C2).
(iii) For the Cu + Cu analysis the simulated hadrons are then embedded in real events in order to account for deterioration of the reconstructed track quality due to high hit multiplicity.
(iv) Reconstruct the resulting particles using the same reconstruction code and track quality cuts used in the real data analysis. (Sec. II D).
(iv) Tune (that is, reweight) the input p_T distributions (from step 1) to match hadron distributions measured in the muon arm (Sec. III C3).

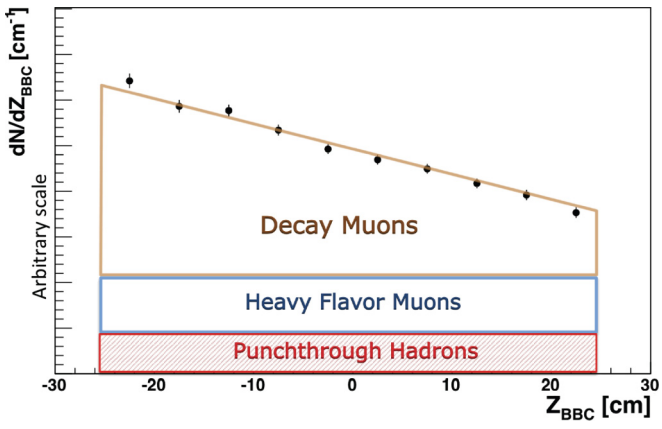

FIG. 5. (Color online) Vertex z distribution of muon candidates reconstructed in the north ($z > 0$) MuID Gap4, relative to the event vertex z distribution (black circles). The vertex z dependencies of the various contributions to the inclusive muon spectra are represented schematically as colored boxes.

1. Input particle distributions

Particle distributions required as input to the hadron cocktail have not been measured over the required y and p_T range at RHIC energies. We therefore use a combination of data from PHENIX, BRAHMS and STAR, together with next-to-leading order (NLO) pQCD calculations to derive realistic parametrizations of these distributions. An exact match to actual distributions is not necessary since the input distributions are re-weighted to match measured-hadron distributions before being used to generate estimates of N_C (Sec. III C3).

We start with the π^0 spectrum in $p + p$ collisions at $y = 0$ measured by PHENIX [29]. This is extrapolated to $y = 1.65$ in two steps. First, an overall scale factor is obtained from a Gaussian parametrization of the charged pion dN/dy distribution measured by BRAHMS [30]. Next, the p_T shape is softened using a parametrization of the ratio of unidentified hadron p_T spectra measured by BRAHMS at $\eta = 0$ and $\eta = 1.65$ [31,32]. These two steps can be written analytically as

$$\begin{aligned} &dN/dp_T(\pi^{\pm}, y = 1.65) \\ &\quad = dN/dp_T(\pi^0, y = 0) \times \exp\left[-\tfrac{1}{2}(1.65/2.25)^2\right] \\ &\qquad \times [1 - 0.1(p_T[\mathrm{GeV}/c] - 1)]. \end{aligned} \tag{7}$$

We next extrapolate this spectrum over the range $1.0 \leqslant y \leqslant 2.4$ using a series of next-to-leading order (NLO) calculations [33] to obtain the ratio $\frac{dN/dp_T(\pi^{\pm},y)}{dN/dp_T(\pi^{\pm},y=1.65)}$. Figure 6 shows a comparison of the hadron cocktail input for charged pions compared to measured charged-pion distributions at $y = 0$ and $y = 2.95$. Spectra for other hadron species in the cocktail are obtained by multiplying the parameterized pion spectra by parametrizations of measured values of hadron-to-pion ratios as a function of p_T.

With 8–11 interaction lengths of material prior to MuID Gap4, approximately 4000 hadrons must be simulated to obtain a single hadron reconstructed as a muon. Given this level of rejection, it is very CPU intensive to generate a sufficient sample of high-p_T hadrons using realistic p_T

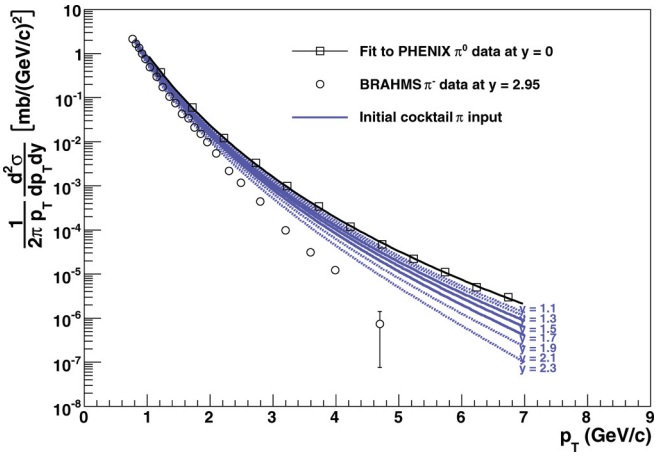

FIG. 6. (Color online) Pion cross sections as a function of pt used as initial hadron cocktail input, for several rapidity intervals in $[1.0, 2.2]$ (blue lines) compared to a fit to the PHENIX π^0 data at $y = 0$ [29] (black line, open black circles) and BRAHMS π^- data at $y = 2.95$ [34] (open black circles).

spectra. A standard technique is to throw particles with a flat p_T spectrum and then weight them with a realistic distribution. However, interactions in the absorber in front of the MuTr and decays in the MuTr volume can both result in particles being reconstructed with incorrect momentum. Due to the steeply falling nature of the p_T spectrum, tracks with low momentum and incorrectly reconstructed with a higher momentum can have a significant contribution at high p_T, with respect to properly reconstructed tracks. As a compromise designed to ensure statistically robust samples of both tracks with *initial* high p_T and with *misreconstructed* high p_T, we multiply the realistic p_T distributions by p_T^2 to form the simulation input p_T distributions and reweight the output of the simulation by $1/p_T^2$ to recover the initial distribution.

The particles in the primary hadron sample used as input to each hadron cocktail package are generated as follows:

(i) The particle type and rapidity are chosen based on dN/dy values obtained by integrating the unweighted p_T distributions described above.
(ii) The particle's transverse momentum is chosen within the range $0.8 \leqslant p_T \leqslant 8$ GeV/c using the p_T^2-weighted p_T distributions described above.
(iii) Since the muon spectrometer acceptance shows little dependence on the vertex z position, the particle's z origin is chosen from a flat distribution over the range $-35 \leqslant z \leqslant 35$ cm.
(iv) The particle's azimuthal angle, ϕ, is chosen from a flat distribution over 2π.

2. *Hadron cocktail packages*

Modeling hadron propagation through thick material is known to be difficult and neither hadron shower code available in GEANT3 (G-FLUKA and GHEISHA) is able to reproduce measured data in the PHENIX muon arms. The approach we have chosen to circumvent this issue is to produce a range of background estimates using a set of hadron cocktails (referred to as *packages*), each of which uses one of the GEANT hadron shower codes and a different, modified, value of the hadron-iron interaction cross section. The set of background estimates are then combined in a weighted fashion to extract central values for production yields, R_{AA}, and the contribution to the systematic uncertainty on these quantities due to the uncertainty in hadron propagation.

Using the default hadron-iron cross section, FLUKA simulations produce more muon candidates than GHEISHA simulations; therefore, the FLUKA cross sections are increased relative to the default and the GHEISHA cross sections are decreased. The cross-section modifications are referred to in terms of percentage, so a 6% increase is referred to as 106%. Five packages are used in this analysis: FLUKA105 (or FL105), FL106, FL107, GHEISHA91 (or GH91), and GH92.

3. *Tuning the hadron cocktail packages*

To tune and validate a given hadron-cocktail package we can compare its output to three measured-hadron distributions as follows:

(i) The p_T distribution of tracks that stop in MuID Gap2, with p_z larger than a given minimum value.
(ii) The p_T distribution of tracks that stop in MuID Gap3, with p_z larger than a given minimum value.
(iii) The vertex z distribution of reconstructed tracks, normalized to the collision-vertex distribution.

Particles that stop in MuID Gap2 or Gap3 are those tracks for which no hit is found in the downstream gaps (Gap3 and/or Gap4). Figure 7 shows the longitudinal-momentum (p_z) distribution of tracks stopping in MuID Gap3 obtained using a given hadronic cocktail. Decay muons are characterized by a sharp peak, corresponding to electromagnetic energy loss in the absorber material. Note that the same peak would be obtained for muons from heavy-flavor decay. In contrast, hadrons are characterized by a broad shoulder that extends to much larger values of p_z. For $p_z > p_z^{\rm min}$ (with $p_z^{\rm min} \approx 3$ GeV/c in this example) one obtains a clean hadron sample. The hadron input p_T distributions can then be tuned so that a good match

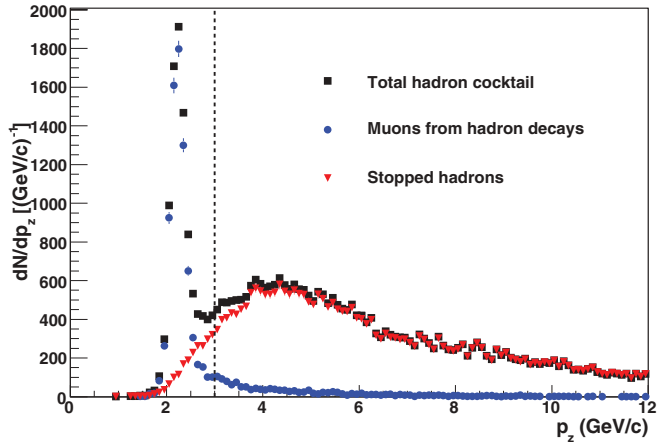

FIG. 7. (Color online) Simulated p_z distributions for particles that stop in MuID Gap3: (black squares) all particles; (red triangles) stopped hadrons; (blue circles) decay muons.

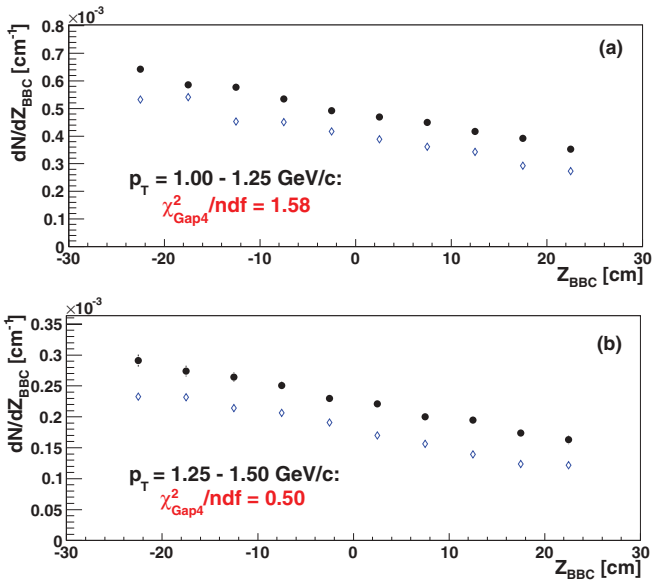

FIG. 8. (Color online) Vertex z distribution of tracks reconstructed in the north ($z > 0$) MuID Gap4 for two transverse-momentum bins. The real data (black solid circles) are compared to a given hadron-cocktail package (blue open diamonds). The offset between data and the hadron cocktail is the contribution from heavy-flavor decays. The χ^2_{Gap4} is defined in the text.

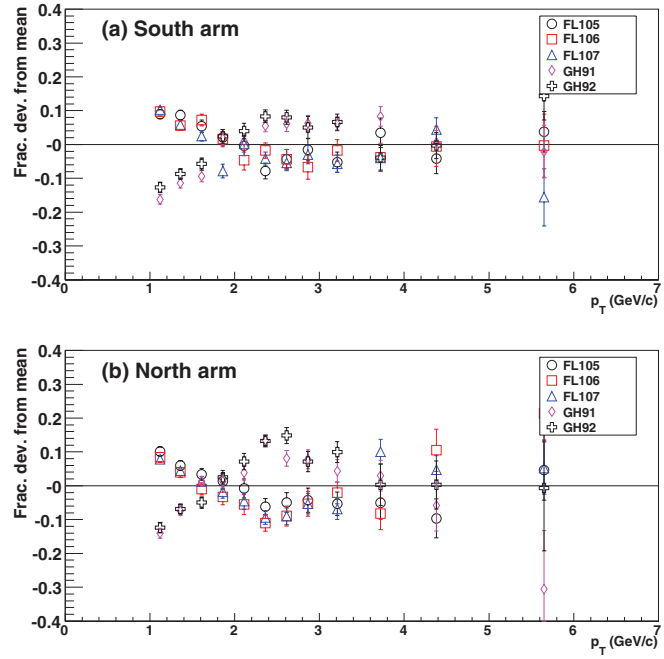

FIG. 9. (Color online) Relative dispersion between the N_C yields obtained with the five hadron cocktails for the $p + p$ analysis. Each hadron cocktail package is compared to the mean of the five packages for the south (a) and north (b) muon arm.

between the number of stopped hadrons in the simulation and in real data is achieved in each p_T bin.

Figure 8 shows dN_μ/dz_{BBC} (the z vertex distributions of tracks, which reach the MuID Gap4 in the north muon arm (located at positive z), normalized by the event vertex distribution $dN_{\text{evt}}/dz_{\text{BBC}}$), for real data and hadron-cocktail simulations in two muon-p_T ranges. The approximately linear dependence on z_{BBC} is entirely due to the contribution of muons from light hadrons decaying before the muon-tracker front absorber. Muons from short-lived heavy-flavor hadrons have no measurable dependence on z_{BBC} and their contribution to the real-data sample is the source of the vertical offset between the hadron cocktail and the real-data distributions. Therefore, the hadron-cocktail package can be tuned by matching the slopes of these two distributions in each p_T bin. The quality of this match is quantified by

$$\chi^2_{\text{Gap4}}(p_T) = \sum_{i=1}^{N_{\text{bins}}} \frac{(\Delta N_i - \overline{\Delta N})^2}{\sigma_i^2 + \sigma_{\text{mean}}^2}, \tag{8}$$

where N_{bins} is the number of z_{BBC} bins, $\Delta N_i = dN_I/dz_{\text{BBC}} - dN_C/dz_{\text{BBC}}$ is the difference between the data and simulation for the i^{th} z_{BBC} bin, $\overline{\Delta N}$ is the average difference over the entire z_{BBC} range, σ_i and σ_{mean} are the statistical uncertainties of ΔN_i and $\overline{\Delta N}$, respectively.

Tuning of each hadron-cocktail package is achieved by iteratively selecting a set of p_T-dependent weights (applied to each track's thrown p_T) that simultaneously optimizes the agreement between data and simulation for the three distributions described above. Applying these weights to those simulated hadron tracks that reach MuID Gap4 determines the corresponding hadron contribution to the inclusive muon yield [N_C, Eq. (3)].

Figure 9 shows the relative dispersion between N_C values obtained for the five different hadron cocktail packages used for the $p + p$ analysis, as a function of p_T. For both muon arms, the largest differences exist between the GHEISHA and FLUKA cocktail packages for $p_T < 2$ GeV/c, with a spread of about 20%. For $p_T > 3$ GeV/c, most of the dispersion between the packages is due to increased statistical uncertainty in the data yields used to tune the hadron cocktail.

4. *Systematic uncertainties associated with individual hadron cocktail packages*

There are two systematic uncertainties associated with a given hadron cocktail package:

σ_{SystPack} The uncertainty associated with the implementation of the hadron cocktail packages. It is composed of two components: (1) the uncertainty in the background calculation due to the uncertainty in the true K/π ratio, conservatively estimated at 15% and correlated between the two arms, and (2) the uncertainty in the background calculation due to potential errors in the track-depth determination arising from incorrect association of a hit unrelated to the track and/or detector inefficiencies. This uncertainty was evaluated using Monte Carlo simulations. It is arm-independent and amounts to 10%. These two contributions are uncorrelated and added in quadrature.

$\sigma_{\text{PackMismatch}}$ The uncertainty that characterizes, as a function of p_T, the ability of a given hadron cocktail package to reproduce the measured distributions described in the previous section. To evaluate this uncertainty the cocktail

is tuned 3 times, each time matching one of the three measured-hadron distributions perfectly. The dispersion between the resulting background yields (N_C) obtained with these three different tunings, along with the central value for N_C obtained using the simultaneous tuning described above, is assigned to $\sigma_{\text{PackMismatch}}$. A different value is calculated for each muon arm, each p_T and centrality bin, and each of the five hadron cocktail packages. Mathematical details of the calculation are outlined in Sec. III G. Since the optimization is arm independent, this uncertainty is uncorrelated between the two muon arms. The magnitude of this uncertainty varies from 10 to 20% depending on the muon arm and the p_T bin.

D. Other background sources

In addition to the hadronic background, other background sources include muons from heavy-flavor-resonance leptonic decay (e.g., χ_c, J/ψ, ψ', and the Υ family); muons from Drell-Yan; and muons from light vector meson decay (ρ, ϕ, and ω).

These three sources contribute significantly less to the inclusive yields than the backgrounds from light hadrons. Monte Carlo simulations performed in the same manner as in Ref. [5] show that their contribution to the final heavy-flavor muon p_T spectrum is less than 5% in the p_T range used for this analysis and they have negligible impact with respect to the other sources of systematic uncertainties.

E. Acceptance and efficiency corrections

Acceptance and efficiency corrections are evaluated using simulated single muons, propagated through the detector using the PHENIX GEANT3 simulation and reconstructed with the same analysis code and the same track quality cuts used for the real data analysis. These corrections account for the detector's geometrical acceptance and inefficiencies (for example, due to tripped high-voltage channels or dead front-end electronic channels). They also account for the muon trigger, reconstruction code, and analysis cut inefficiencies.

The hit multiplicity in the MuTr for Cu + Cu collisions is much higher than for $p + p$ collisions and for the single muon simulations. To account for deterioration of the reconstruction efficiency in presence of such high-multiplicity events, simulated single muon events are embedded into real data Cu + Cu events before running the reconstruction and evaluating the $A\epsilon$ correction. (The maximum efficiency loss, for the highest multiplicity Cu + Cu collisions, is 16%.)

A reference run, representative of a given data-taking period, is chosen to define the detector's response to particles passing through it. This includes notably the list of inactive high-voltage and electronic channels. Remaining run-to-run variations with respect to this reference run are small due to the overall stability of the detector's performance and are included in the systematic uncertainties ($\sigma_{\text{run to run}} = 2\%$).

A comparison between the hit distributions in the MuTr and the MuID obtained for the reference run in real data and simulations is used to assign an additional systematic error on our ability to reproduce the real detector's response in the simulations. Areas with unacceptable discrepancies are removed from both the simulations and the real data using fiducial cuts. Remaining discrepancies are accounted for with a 8% systematic uncertainty for the MuTr and 4.5% for the MuID.

Another systematic uncertainty, $\sigma_{\text{p-scale}}$, is assigned to a possible systematic bias between the particle's reconstructed momentum and its real momentum. This uncertainty is estimated by comparing the measured J/ψ invariant mass (using the dimuon invariant mass distribution) and its Particles Data Group (PDG) value. This uncertainty amounts to ~1.5%.

Table II summarizes the acceptance and efficiency related uncertainties, which sum quadratically to 9.5%.

TABLE II. Uncertainties in the acceptance and efficiency corrections. Individual components are added in quadrature to obtain the total value of $\sigma_{A\epsilon}$.

	Component	Value
σ_{MuTr}	MuTr station data/MC	8%
σ_{MuID}	MuID Gap4 efficiency uncertainty	4.5%
$\sigma_{\text{run to run}}$	Run-to-run variation	2%
$\sigma_{\text{p-scale}}$	Momentum scale	1.5%
$\sigma_{A\epsilon}$	Total	9.5%

F. Systematic uncertainties

This section summarizes systematic uncertainties associated with this analysis, most of which have been described in previous sections:

(i) Systematic uncertainties associated with individual hadron cocktail packages, σ_{SystPack} and $\sigma_{\text{PackMismatch}}$ (Sec. III C4);
(ii) Systematic uncertainty resulting from the dispersion of the results obtained with the different hadron cocktail packages (introduced in Sec. III C2, mathematical details in Sec. III G);
(iii) Systematic uncertainty on the acceptance and efficiency correction factors, $\sigma_{A\epsilon}$ (Sec. III E and Table II).

These systematic uncertainties are calculated independently for each arm, p_T bin, and centrality bin.

The first three uncertainties listed above (first two items) are related to the hadronic background estimate and are combined to form a σ_{model} systematic uncertainty, following a method described in Sec. III G.

For invariant cross-section measurements (in $p + p$ collisions) and measurements of R_{AA}, one must add to the uncertainties above the systematic uncertainty on the $p + p$ inelastic cross section seen by the minimum bias trigger, $\sigma^{pp}_{\epsilon^{c\bar{c}\to\mu}_{\text{BBC}}} = 9.6\%$. For R_{AA} measurements, one must also add the systematic uncertainty on the mean number of binary collisions (N_{coll}) in each centrality bin, as provided by the Glauber calculation used to determine this quantity.

Table III summarizes the systematic uncertainties in this analysis.

TABLE III. Uncertainties in the single muon analysis. The individual components contribute to the final uncertainty as discussed in Sec. III G.

	Component	Value
$\sigma_{\text{PackMismatch}}$	Package mismatch	varies, 10–20%
σ_{SystPack}	Single package uncertainty	18%
$\sigma_{A\epsilon}$	Acceptance and efficiency	9.5%
$\sigma^{pp}_{\epsilon^{c\bar{c}\to\mu}_{\text{BBC}}}$	$\epsilon^{c\bar{c}\to\mu}_{\text{BBC}}$	9.6%
$\sigma_{N_{\text{coll}}}$	N_{coll}	varies, 10–13%

G. Determination of the central value for heavy-flavor-muon production yields and R_{AA}

This section details the procedure used to combine the results from multiple hadron cocktail packages to obtain the central values for the p_T spectra and R_{AA} and to propagate associated systematic uncertainties. This discussion includes the definition of $\sigma_{\text{PackMismatch}}$ and σ_{model}. Throughout this section, the variable Q is used to represent either the invariant yield or R_{AA} for a given p_T and centrality bin; the procedure is the same for both, except where noted explicitly.

(i) For each p_T bin i, hadron cocktail package j, and package tuning k, we calculate the value $Q_{i,j,k}$ where
$k = 1$ is the *optimal* tuning that best matches all three hadron distributions simultaneously (see Sec. III C3);
$k = 2$ is the tuning that best reproduces the p_T distribution of particles stopping in MuID Gap2;
$k = 3$ is the tuning that best reproduces the p_T distribution of particles stopping in MuID Gap3;
$k = 4$ represents the tuning that best reproduces the vertex z distribution of particles reaching MuID Gap4.
The tuning $k = 1$ is used for the central value, whereas the other tunings are used to establish the systematic uncertainty for a single hadron cocktail package due to its inability to completely describe measured-hadron distributions.

(ii) The package mismatch contribution to the uncertainty on the measurement $Q_{i,j,k}$ is estimated by the standard deviation between the four tunings, k,

$$\sigma^2_{\text{PackMismatch},i,j} = \frac{1}{4}\sum_{k=1}^{4}(Q_{i,j,k} - \langle Q_{i,j,k}\rangle)^2. \quad (9)$$

(iii) For each p_T bin i and package j, the associated total uncertainty $\sigma_{i,j}$ is computed,

$$\sigma^2_{i,j} = \sigma^2_{\text{StatData},i} + \sigma^2_{\text{StatPack},i,j} + \sigma^2_{\text{SystPack},i} + \sigma^2_{\text{PackMismatch},i,j} + \sigma^2_{A\epsilon,i}, \quad (10)$$

where the first two contributions, $\sigma^2_{\text{StatData},i}$ and $\sigma^2_{\text{StatPack},i}$, are the statistical uncertainties on the data and on the simulation and all other terms have already been introduced in previous sections.

(iv) Using $\sigma_{i,j}$ from step 3 we calculate the weighted mean of the $Q_{i,j}$ values obtained for the optimal tuning ($k = 1$) of the different packages, j, in each p_T bin, i,

$$\langle Q_i\rangle = \sum_{j=1}^{5} w_{i,j}\, Q_{i,j,k=1}, \quad (11)$$

where

$$w_{i,j} \equiv \frac{1/\sigma^2_{i,j}}{\sum_{j=1}^{5} 1/\sigma^2_{i,j}}. \quad (12)$$

(v) The total uncertainty on the final measurement is the variance of the weighted mean,

$$\text{Var}(\langle Q_i\rangle) = \sum_{j=1}^{5} w^2_{i,j}\sigma^2_{i,j} + 2\sum_{j<m}^{5} w_{i,j}w_{i,m}\sigma^2_{\text{common},i}, \quad (13)$$

where $\sigma_{\text{common},i}$ is the part of the total uncertainty that is correlated among different packages,

$$\sigma^2_{\text{common},i} \equiv \sigma^2_{\text{StatData},i} + \sigma^2_{\text{SystPack},i} + \sigma^2_{A\epsilon,i}. \quad (14)$$

(vi) The total uncertainty $\text{Var}(\langle Q_i\rangle)^{1/2}$ is split into statistical and systematic components,

$$\text{Var}(\langle Q_i\rangle) = \sigma^2_{\text{StatCombined},i} + \sigma^2_{\text{SystCombined},i} \quad (15)$$

with

$$\sigma^2_{\text{StatCombined},i} = \sigma^2_{\text{StatData},i} + \frac{1}{5}\sum_{j=1}^{5}\sigma^2_{\text{StatPack},i,j} \quad (16)$$

and (by construction)

$$\sigma^2_{\text{SystCombined},i} \equiv \text{Var}(\langle Q_i\rangle) - \sigma^2_{\text{StatCombined},i} \quad (17)$$

so the final measurement, in a given muon arm, is written

$$\langle Q_i\rangle \pm \sigma_{\text{StatCombined},i} \pm \sigma_{\text{SystCombined},i}. \quad (18)$$

The systematic uncertainty can be further decomposed to quantify $\sigma_{\text{model},i}$, the contribution from the uncertainty due to the hadronic cocktail model uncertainties,

$$\sigma^2_{\text{SystCombined},i} = \sigma^2_{\text{model},i} + \sigma^2_{A\epsilon,i}. \quad (19)$$

$\sigma_{\text{SystCombined},i}$ is p_T- and arm dependent, varying from 14 to 23%, from which we see that $\sigma_{\text{model},i}$ varies between 10 and 21%.

(vii) The independent north and south measurements are combined using

$$\langle Q_i\rangle = \sum_{j=1}^{2} w_{i,j}\, Q_{i,j}, \quad (20)$$

where i is the index of the p_T bin, j the arm index, and $w_{i,j}$ a weight calculated in the same manner as in Eq. (12), using the following total uncertainty on the measurement $Q_{i,j}$,

$$\sigma^2_{i,j} = \sigma^2_{\text{StatCombined},i,j} + \sigma^2_{\text{SystCombined},i,j}, \quad (21)$$

which is identical to the expression of Eq. (15) but explicitly includes the arm index, j.

The total uncertainty on the arm-averaged Q_i value is calculated in a manner similar to Eq. (13),

$$\mathrm{Var}(\langle Q_i \rangle) = \sum_{j=1}^{2} w_{i,j}^2 \sigma_{i,j}^2 + 2 \sum_{j<m}^{2} w_{i,j} w_{i,m} \sigma^2_{\text{arm common},i}, \tag{22}$$

where $\sigma^2_{\text{arm common},i}$ is the systematic uncertainty common to both muon arms due to uncertainty on cocktail input. For convenience, this uncertainty is again split into a statistical contribution $\sigma_{\text{StatCombined},i}$ and a systematic contribution $\sigma_{\text{SystCombined},i}$ defined by

$$\sigma^2_{\text{SystCombined},i} \equiv \mathrm{Var}(\langle Q_i \rangle) - \sigma^2_{\text{StatCombined},i} \tag{23}$$

so the final, arm-averaged, measurement of Q_i is written,

$$\langle Q_i \rangle \pm \sigma_{\text{SystCombined},i} \pm \sigma_{\text{StatCombined},i}. \tag{24}$$

As already noted in Sec. III F, for invariant cross section measurements (in $p+p$ collisions) and R_{AA} measurements one must add the systematic uncertainty on the $p+p$ inelastic cross section seen by the minimum bias trigger, $\sigma^{pp}_{\epsilon^{c\bar{c}\to\mu}_{\text{BBC}}}$ in quadrature to the uncertainties above. For R_{AA} measurements one must also add the systematic uncertainty on the mean number of binary collisions N_{coll} in each centrality bin.

IV. RESULTS

A. Heavy-flavor muon p_T distributions in $p+p$ and Cu + Cu collisions

Figure 10 shows the production cross section of negatively charged muons from decays of heavy-flavor mesons as a function of p_T in $p+p$ collisions at $\sqrt{s} = 200$ GeV. Vertical bars correspond to statistical uncertainties. Boxes correspond to the systematic uncertainties calculated following the steps

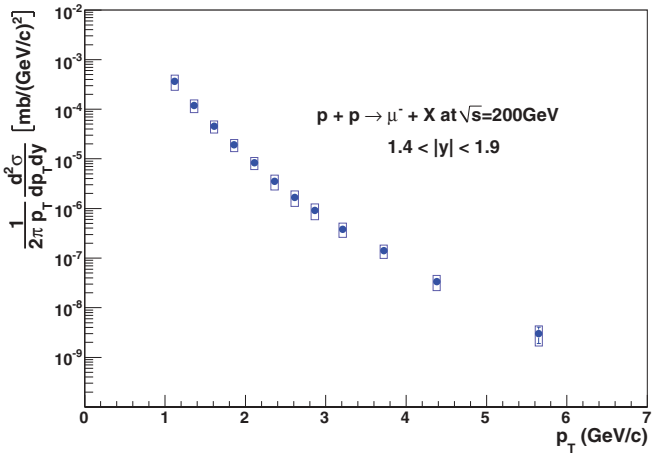

FIG. 10. (Color online) Production cross section of negative muons from heavy-flavor meson decay as a function of p_T in $p+p$ collisions at $\sqrt{s} = 200$ GeV. Vertical errors bars and boxes correspond to statistical and systematic uncertainties, respectively, as described in the text.

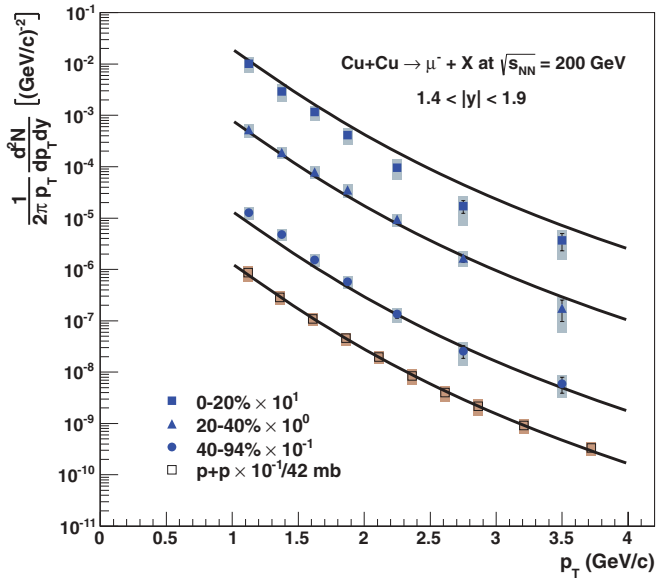

FIG. 11. (Color online) Invariant production yields of negative muons from heavy-flavor meson decay as a function p_T in $p+p$ collisions at $\sqrt{s} = 200$ GeV (open squares) and in Cu + Cu collisions for three different centrality bins (40–94%, 20–40%, and 0–20%), scaled by powers of 10 for clarity (filled circles). The solid line associated with each set of points corresponds to a fit to the $p+p$ invariant yield distribution described in the text, scaled by the appropriate number of binary collisions N_{coll} when comparing to the Cu + Cu measurements.

described in Sec. III G. The measurements from both muon arms have been combined to reduce the overall uncertainty. Measured values for each p_T bin are listed in the Appendix (Table IV).

Figure 11 shows the invariant yield of negative muons from heavy-flavor meson decay for all analyzed Cu + Cu centrality bins, compared to the invariant yield measured in $p+p$ collisions. The solid lines correspond to a fit to the $p+p$ data using the function $A[1+(p_T/B)^2]^{-4.2}$, similar to the one used in Ref. [35], scaled by the average number of binary collisions N_{coll} for each Cu + Cu centrality bin. For peripheral (40–94% centrality) and midcentral (20–40% centrality) Cu + Cu collisions, reasonable agreement is observed between the measurement and the scaled fit to the $p+p$ data. In contrast, central Cu + Cu collisions (0–20%) exhibit a systematic suppression in the yield of negative muons from heavy-flavor decay relative to binary collision scaling. This is quantified in Sec. IV C).

B. Charm cross section, $d\sigma_{c\bar{c}}/dy|_{\langle y\rangle=1.65}$ in $p+p$ collisions

The $p+p$ heavy-flavor muon p_T distribution is used to estimate the charm differential production cross section, $d\sigma_{c\bar{c}}/dy$ at forward rapidity ($\langle y \rangle = 1.65$), as described in detail in Ref. [27]. The muon p_T spectrum measured in $p+p$ collisions spans from $p_T = 1$ to 7 GeV/c. Estimation of the full charm charm cross section requires a theoretical calculation in order to extrapolate the measurement down to $p_T = 0$ GeV/c. A set of fixed-order-plus-next-to-leading-log (FONLL) [36,37] calculations have been used in this analysis.

The charm-production cross section $d\sigma_{c\bar{c}}/dy$ is derived from the heavy-flavor muon cross section using

$$d\sigma_{c\bar{c}}/dy = \frac{1}{BR(c \to \mu)} \frac{1}{C_{l/D}} \frac{d\sigma_{\mu^-}}{dy}, \quad (25)$$

where $BR(c \to \mu)$ is the total muon branching ratio of charm and is fixed to 0.103 in FONLL; $C_{l/D}$ is a kinematic correction factor, also provided by the FONLL calculation, which accounts for the difference in rapidity distributions between leptons and D mesons; and $d\sigma_{\mu^-}/dy$ is the total cross section for negative muons from heavy-flavor meson decay, integrated over p_T and estimated by extrapolating our measurement down to $p_T = 0$ GeV/c using the FONLL calculation.

1. Extrapolation of the data for $p_T < 1.0$ GeV/c

Low p_T muons dominate the integrated heavy-flavor muon cross section due to the power-law-like behavior of the p_T distribution (Fig. 10): According to the central value of the FONLL calculation, the integrated charm cross section for $p_T^{\mu} > 1$ GeV/c represents about 6% of the total. Additionally, the contribution of bottom quark decays to the heavy-flavor muon p_T distribution becomes increasingly relevant for $p_T >$ 4 GeV/c but has a negligible contribution to the integral and is ignored hereafter.

The measured spectrum and the scaled FONLL prediction agree to within ±10% for all data points [27]. Therefore, extrapolation of the measured heavy-flavor muon p_T spectra down to $p_T = 0$ GeV/c using FONLL is given by

$$d\sigma_{c\bar{c}}/dy|^{\text{PHENIX}} = d\sigma_{c\bar{c}}/dy|^{\text{FONLL}} \alpha^{\text{FONLL}}, \quad (26)$$

where α^{FONLL} is a constant determined by fitting the central values of the FONLL p_T distribution to the data for $p_T >$ 1 GeV/c. It amounts to 3.75 and is used in determining the central value for PHENIX muons shown in Fig. 12.

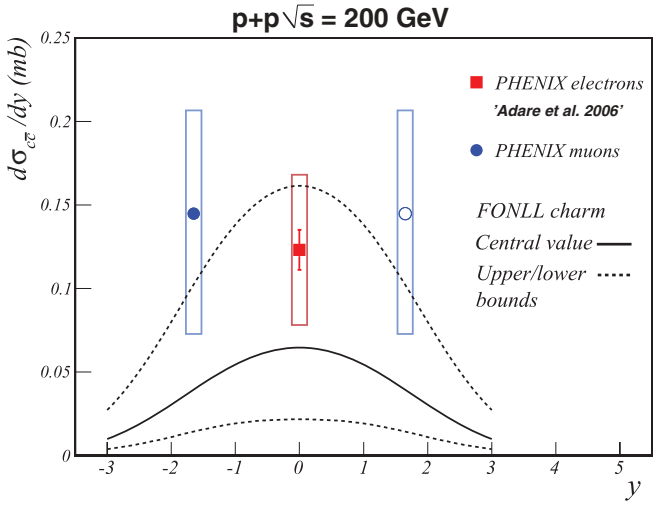

FIG. 12. (Color online) $c\bar{c}$ production cross section as a function of rapidity in $p + p$ collisions, measured using semileptonic decay to electrons from Adare *et al.* [38] (solid square) and to muons (solid circle).

2. Systematic uncertainties on $d\sigma_{c\bar{c}}/dy|_{\langle y\rangle=1.65}$

The total systematic uncertainty assigned to $d\sigma_{c\bar{c}}/dy|_{\langle y\rangle=1.65}$ is a combination of experimental and theoretical uncertainties, added in quadrature. The experimental systematic uncertainty on the integral above $p_T > 1$ GeV/c is determined by the appropriate quadrature sum of the systematic uncertainties on the individual p_T points. This uncertainty is up-down symmetric and is equal to 32%.

The theoretical uncertainty for $d\sigma_{c\bar{c}}/dy|_{\langle y\rangle=1.65}$ originates from the FONLL uncertainties, which are determined by varying the factorization scale, μ_F, the renormalization scale, μ_R, and the charm quark mass. Other contributions, such as fragmentation and parton distribution functions, are smaller and neglected in this analysis. The FONLL upper and lower spectra, obtained by variation of the FONLL parameters [27], are treated as approximations for a one standard deviation systematic variation of the magnitude and shape of the prediction. The ratio of the measured p_T spectra for $p_T > 1$ GeV/c to the upper and lower FONLL spectra are fit independently to determine the corresponding two normalization factors. The difference between these two normalization factors is then used as a theoretical uncertainty. This uncertainty is asymmetric and amounts to $^{+29}_{-37}$%. These FONLL systematic uncertainties are consistent with those of a previous study [27], which examined the different p_T spectra obtained by varying the FONLL parameters, $1.3 < M_c[\text{GeV}/c^2] < 1.7$, $0.5 < \mu_R/m_T < 2$, $0.5 < \mu_F/m_T < 2$, with m_T representing transverse mass. The different predicted theoretical p_T spectra ranged within an envelope of ±35% relative to the central spectrum.

3. Integrated charm production cross section at $\langle y\rangle = 1.65$ in $p + p$ collisions

The integrated charm-production cross section at forward rapidity ($\langle y\rangle = 1.65$) obtained with this method is

$$d\sigma_{c\bar{c}}/dy|_{\langle y\rangle=1.65} = 0.139 \pm 0.029\ (\text{stat})^{+0.051}_{-0.058}\ (\text{syst})\ \text{mb}. \quad (27)$$

This measurement is shown in Fig. 12, together with the measurement performed by PHENIX at midrapidity [38] and the FONLL central value and upper and lower bounds, based on Ref. [39]. The full circle, located at $y = -1.65$, corresponds to the combined measurement performed in both muon arms. The open circle, located at $y = 1.65$, corresponds to its mirror image.

C. Heavy-flavor muon R_{AA} in Cu + Cu collisions as a function of p_T

Figure 13 shows $R_{AA}(p_T)$ for muons from heavy-flavor meson decay in Cu + Cu collisions as a function of muon p_T for three centrality bins (40–94%, 20–40%, and 0–20%). As was the case for invariant yields and cross sections, the two independent measurements obtained with each muon arm are statistically combined, following the method discussed in Sec. III G. Vertical bars correspond to the quadrature sum of statistical uncertainties and point-to-point correlated systematic uncertainties; boxes centered on the data points correspond to point-to-point correlated systematic uncertainties and the

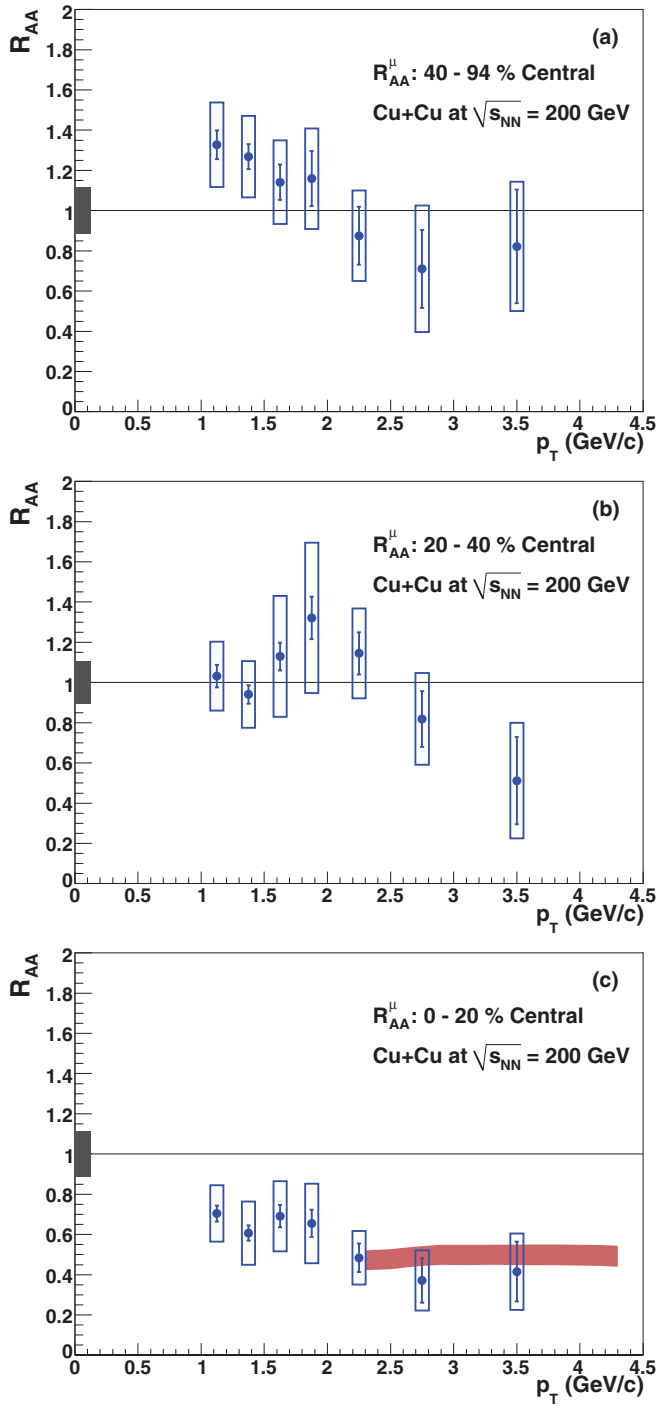

FIG. 13. (Color online) Transverse-momentum distribution of R_{AA} for negative muons from heavy-flavor meson decay in Cu + Cu collisions in the following centrality bins: 40–94% (a), 20–40% (b), and 0–20% (c). Also shown in (c) is a theoretical calculation from Refs. [40,41], discussed in Sec. V.

vertical gray band centered on unity corresponds to the uncertainty on $N_{\rm coll}$, as listed in Table I. Also shown in the bottom panel of Fig. 13 is a theoretical calculation from Refs. [40,41], discussed in Sec. V. The measured values for each p_T bin and each centrality bin are listed in the Appendix (Table V).

V. DISCUSSION AND CONCLUSIONS

The measurement of heavy-flavor muon production in $p + p$ collisions at $\sqrt{s} = 200$ GeV reported in this paper is a significant improvement over the previous PHENIX published result [25]. The transverse-momentum range of the present measurement is extended to $p_T = 7$ GeV/c (compared to $p_T = 3$ GeV/c in the previous analysis). The differential production cross section is integrated over p_T to calculate a charm-production cross section at forward rapidity of $d\sigma_{c\bar{c}}/dy|_{\langle y\rangle=1.65} = 0.139 \pm 0.029\ (\text{stat})^{+0.051}_{-0.058}$ (syst) mb. This cross section is compatible with a FONLL calculation within experimental and theoretical uncertainties. It is also compatible with expectations based on the corresponding midrapidity charm-production cross section measured by PHENIX.

Muons from heavy-flavor meson decay have also been measured in Cu + Cu collisions at $\sqrt{s_{NN}} = 200$ GeV/c, in the same rapidity and momentum range. This allows determination of the heavy-flavor muon R_{AA} as a function of p_T in three centrality bins, 40–94%, 20–40%, and 0–20%. As shown in Fig. 13, no clear suppression is observed across most of the transverse-momentum range for muon yields measured in peripheral (40–94%) and midcentral (20–40%) Cu + Cu collisions compared to $N_{\rm coll}$-scaled $p + p$ collisions. However, heavy-flavor muon production is significantly suppressed for central Cu + Cu collisions (0–20%), with the largest effect observed for $p_T > 2$ GeV/c. Interestingly, as demonstrated in Fig. 14, the level of suppression for these higher-p_T heavy-flavor muons (the last red point on right) is comparable to the level of suppression observed for high-p_T nonphotonic electrons measured at midrapidity in the most central Au + Au collisions (the last blue point on right). One expects the Bjorken energy density of the matter produced in the midrapidity region in the most central Au + Au collisions to be at least twice as large as that of the matter produced in the forward rapidity region in most central Cu + Cu collisions

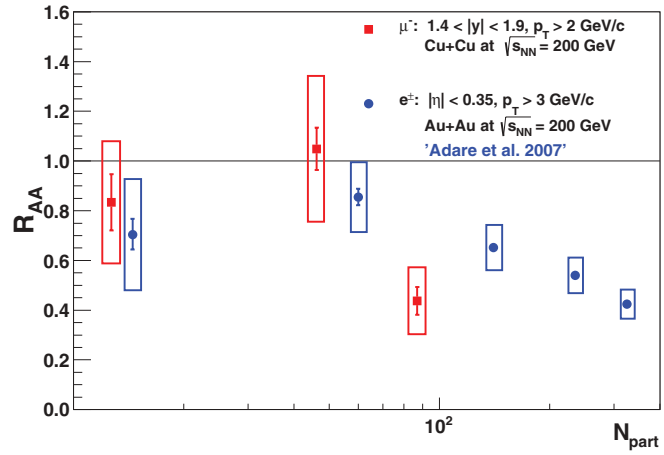

FIG. 14. (Color online) Comparison of R_{AA} as a function of $N_{\rm part}$ between negative muons from heavy-flavor decay reconstructed at forward rapidity ($1.4 < y < 1.9$) and $p_T > 2$ GeV in Cu + Cu collisions (red squares) and nonphotonic electrons reconstructed at midrapidity and $p_T > 3$ GeV in Au + Au collisions from Adare *et al.* [4]) (blue circles).

[26,42]. Therefore, the large suppression observed in Cu + Cu collisions suggests significant (cold) nuclear effects at forward rapidity in addition to effects due to strongly interacting partonic matter.

As shown in the Fig. 13(c), the suppression of heavy-flavor muon production for central Cu + Cu collisions is consistent with a recent theoretical calculation performed at the same rapidity ($y = 1.65$) for $p_T > 2.5$ GeV/c [40,41]. This calculation includes effects of heavy-quark energy loss (both elastic and inelastic) and in-medium heavy meson dissociation. Additionally, the calculation accounts for cold nuclear matter effects relevant for heavy-flavor production [43], namely shadowing (nuclear modification of the parton distribution functions of the nucleon) and initial-state energy loss due to multiple scattering of incoming partons before they interact to form the $c\bar{c}$ pair.

New PHENIX inner silicon vertex detectors will greatly improve heavy-flavor production measurements and allow separation of charm and bottom contributions [44,45]. Such measurements will further clarify and guide theoretical understanding of medium-induced energy-loss mechanisms in hot dense partonic matter and ultimately contribute to an improved understanding of QCD matter at extreme energy and density.

ACKNOWLEDGMENTS

We thank the staff of the Collider-Accelerator and Physics Departments at Brookhaven National Laboratory and the staff of the other PHENIX participating institutions for their vital contributions. We acknowledge support from the Office of Nuclear Physics in the Office of Science of the Department of Energy, the National Science Foundation, Abilene Christian University Research Council, Research Foundation of SUNY, and the Dean of the College of Arts and Sciences, Vanderbilt University (USA); Ministry of Education, Culture, Sports, Science, and Technology and the Japan Society for the Promotion of Science (Japan); Conselho Nacional de Desenvolvimento Científico e Tecnológico and Fundação de Amparo à Pesquisa do Estado de São Paulo (Brazil); Natural Science Foundation of China (P. R. China); Ministry of Education, Youth and Sports (Czech Republic); Centre National de la Recherche Scientifique, Commissariat à l'Énergie Atomique, and Institut National de Physique Nucléaire et de Physique des Particules (France); Bundesministerium für Bildung und Forschung, Deutscher Akademischer Austausch Dienst, and Alexander von Humboldt Stiftung (Germany); Hungarian National Science Fund, OTKA (Hungary); Department of Atomic Energy (India); Israel Science Foundation (Israel); National Research Foundation and WCU program of the Ministry Education Science and Technology (Korea); Ministry of Education and Science, Russian Academy of Sciences, Federal Agency of Atomic Energy (Russia); VR and the Wallenberg Foundation (Sweden); the US Civilian Research and Development Foundation for the Independent States of the Former Soviet Union; the US-Hungarian NSF-OTKA-MTA; and the U.S.-Israel Binational Science Foundation.

TABLE IV. Differential-invariant cross section of negative muons from heavy-flavor meson decay for 200 GeV $p + p$ collisions at midrapidity.

p_T (GeV/c)	$1/(2\pi\, p_T)\, d^2\sigma/(dp_T d\eta)$ (mb)	Stat. error	Syst. error
1.12	3.64×10^{-4}	1.55×10^{-5}	1.23×10^{-4}
1.36	1.19×10^{-4}	2.85×10^{-6}	3.39×10^{-5}
1.61	4.57×10^{-5}	1.15×10^{-6}	1.25×10^{-5}
1.86	1.92×10^{-5}	5.39×10^{-7}	5.18×10^{-6}
2.11	8.31×10^{-6}	3.02×10^{-7}	2.27×10^{-6}
2.36	3.52×10^{-6}	1.54×10^{-7}	1.18×10^{-6}
2.61	1.67×10^{-6}	9.21×10^{-8}	5.74×10^{-7}
2.86	9.12×10^{-7}	6.04×10^{-8}	3.18×10^{-7}
3.21	3.83×10^{-7}	2.28×10^{-8}	1.22×10^{-7}
3.72	1.41×10^{-7}	1.24×10^{-8}	4.15×10^{-8}
4.38	3.34×10^{-8}	3.49×10^{-9}	1.12×10^{-8}
5.65	2.99×10^{-9}	1.09×10^{-9}	1.31×10^{-9}

APPENDIX: DATA TABLES

Table IV gives the differential invariant cross section of muons from heavy-flavor decay in $\sqrt{s} = 200$ GeV $p + p$ collisions and corresponds to Fig. 10. Table V gives the R_{AA} of muons from heavy-flavor meson decay for the different centrality bins of $\sqrt{s_{NN}} = 200$ GeV Cu + Cu collisions and corresponds to Fig. 13.

TABLE V. Nuclear-modification factor, R_{AA}, of negative muons from heavy-flavor meson decay as a function of p_T for the specified centrality bins of Cu + Cu collisions at $\sqrt{s_{NN}} = 200$ GeV.

Centrality	p_T (GeV/c)	R_{AA}	Stat. error	Syst. error
0–20%	1.13	6.93×10^{-1}	3.98×10^{-2}	1.87×10^{-1}
	1.38	5.41×10^{-1}	3.49×10^{-2}	1.87×10^{-1}
	1.63	6.57×10^{-1}	5.32×10^{-2}	2.20×10^{-1}
	1.875	6.26×10^{-1}	6.74×10^{-2}	2.28×10^{-1}
	2.25	4.54×10^{-1}	6.90×10^{-2}	1.50×10^{-1}
	2.75	3.61×10^{-1}	1.09×10^{-1}	1.46×10^{-1}
	3.5	3.95×10^{-1}	1.46×10^{-1}	2.00×10^{-1}
20–40%	1.13	1.03	5.59×10^{-2}	2.66×10^{-1}
	1.38	9.32×10^{-1}	4.63×10^{-2}	2.46×10^{-1}
	1.63	1.11	6.95×10^{-2}	3.72×10^{-1}
	1.875	1.34	1.08×10^{-1}	4.59×10^{-1}
	2.25	1.15	1.06×10^{-1}	3.18×10^{-1}
	2.75	8.14×10^{-1}	1.40×10^{-1}	2.80×10^{-1}
	3.5	4.42×10^{-1}	2.03×10^{-1}	2.96×10^{-1}
40–94%	1.13	1.36	7.27×10^{-2}	3.38×10^{-1}
	1.38	1.28	6.26×10^{-2}	3.21×10^{-1}
	1.63	1.16	8.87×10^{-2}	3.08×10^{-1}
	1.875	1.16	1.37×10^{-1}	3.30×10^{-1}
	2.25	8.64×10^{-1}	1.43×10^{-1}	2.73×10^{-1}
	2.75	6.94×10^{-1}	1.92×10^{-1}	3.30×10^{-1}
	3.5	8.09×10^{-1}	2.80×10^{-1}	3.47×10^{-1}

[1] M. J. Tannenbaum, Rep. Prog. Phys. **69**, 2005 (2006).
[2] D. d'Enterria, in *Landolt-Boernstein–Group I Elementary Particles, Nuclei and Atoms Numerical Data and Functional Relationships in Science and Technology*, edited by R. Stock, Relativistic Heavy Ion Physics, Vol. 23 (Springer-Verlag, Berlin, Heidelberg, 2010).
[3] S. S. Adler *et al.* (PHENIX Collaboration), Phys. Rev. Lett. **96**, 032301 (2006).
[4] A. Adare *et al.* (PHENIX Collaboration), Phys. Rev. Lett. **98**, 172301 (2007).
[5] A. Adare *et al.* (PHENIX Collaboration), Phys. Rev. C **84**, 044905 (2011).
[6] M. Djordjevic, M. Gyulassy, and S. Wicks, Phys. Rev. Lett. **94**, 112301 (2005).
[7] N. Armesto *et al.*, Nucl. Phys. A **774**, 589 (2006).
[8] M. Gyulassy and X.-N. Wang, Nucl. Phys. B **420**, 583 (1994).
[9] R. Baier *et al.*, Phys. Lett. B **345**, 277 (1995).
[10] Y. L. Dokshitzer and D. Kharzeev, Phys. Lett. B **519**, 199 (2001).
[11] M. G. Mustafa, Phys. Rev. C **72**, 014905 (2005).
[12] G. D. Moore and D. Teaney, Phys. Rev. C **71**, 064904 (2005).
[13] H. van Hees, V. Greco, and R. Rapp, Phys. Rev. C **73**, 034913 (2006).
[14] A. Adil and I. Vitev, Phys. Lett. B **649**, 139 (2007).
[15] R. Rapp and H. van Hees, arXiv:0903.1096 (2009).
[16] A. Adare *et al.* (PHENIX Collaboration), Phys. Rev. Lett. **98**, 232301 (2007).
[17] A. Adare *et al.* (PHENIX Collaboration), Phys. Rev. Lett. **101**, 122301 (2008).
[18] T. Matsui and H. Satz, Phys. Lett. B **178**, 416 (1986).
[19] A. Andronic *et al.*, Phys. Lett. B **36**, 571 (2003).
[20] B. Svetitsky, Phys. Rev. D **37**, 2484 (1988).
[21] R. L. Thews, Eur. Phys. J. **34**, 97 (2005).
[22] M. L. Miller, K. Reygers, S. J. Sanders, and P. Steinberg, Annu. Rev. Nucl. Part. Sci. **57**, 205 (2007).
[23] K. Adcox *et al.* (PHENIX Collaboration), Nucl. Instrum. Methods A **499**, 469 (2003).
[24] M. Allen *et al.* (PHENIX Collaboration), Nucl. Instrum. Methods A **499**, 549 (2003).
[25] S. S. Adler *et al.* (PHENIX Collaboration), Phys. Rev. D **76**, 092002 (2007).
[26] I. Garishvili, Ph.D. thesis, University of Tennessee, Knoxville (2009).
[27] D. E. Hornback, Ph.D. thesis, University of Tennessee, Knoxville (2008).
[28] R. Brun *et al.*, CERN Program Library Long Write-up W5013 (1994), http://wwwasd.web.cern.ch/wwwasd/geant/.
[29] S. S. Adler *et al.* (PHENIX Collaboration), Phys. Rev. Lett. **91**, 241803 (2003).
[30] F. Videbaek (BRAHMS Collaboration), arXiv:0907.4742 (2009).
[31] B. Samset, Ph.D. thesis, University of Oslo, Norway (2006).
[32] I. Arsene *et al.* (BRAHMS Collaboration), Phys. Rev. Lett. **93**, 242303 (2004).
[33] W. Vogelsang (private communication) (2008).
[34] I. Arsene *et al.* (BRAHMS Collaboration), Phys. Rev. Lett. **98**, 252001 (2007).
[35] J. Yoh *et al.*, Phys. Rev. Lett. **41**, 684 (1978).
[36] M. Cacciari, M. Greco, and P. Nason, J. High Energy Phys. 05 (1998) 007.
[37] M. Cacciari, S. Frixione, and P. Nason, J. High Energy Phys. 03 (2001) 006.
[38] A. Adare *et al.* (PHENIX Collaboration), Phys. Rev. Lett. **97**, 252002 (2006).
[39] M. Cacciari, P. Nason, and R. Vogt, Phys. Rev. Lett. **95**, 122001 (2005).
[40] I. Vitev (private communication) (2011).
[41] R. Sharma, I. Vitev, and B.-W. Zhang, Phys. Rev. C **80**, 054902 (2009).
[42] C.-Y. Wong (private communication) (2009).
[43] I. Vitev, Phys. Rev. C **75**, 064906 (2007).
[44] R. Noucier *et al.*, Nucl. Instrum. Methods B **261**, 1067 (2007).
[45] J. S. Kapustinsky *et al.*, Nucl. Instrum. Methods A **617**, 546 (2010).